

Crystallization Characteristics and Chemical Bonding Properties of Nickel Carbide Thin Film Nanocomposites

Andrej Furlan^{1,*}, Jun Lu¹, Lars Hultman¹, Ulf Jansson² and Martin Magnuson^{1,**}

¹*Department of Physics, IFM, Thin Film Physics Division,
Linköping University, SE-58183 Linköping, Sweden.*

²*Department of Chemistry - Ångström Laboratory,
Uppsala University, Box 538, SE-751 21 Uppsala Sweden. and*

**Present address: AMB Industry, Kvarnvägen 26, 361 93 Broakulla, Sweden.*

(Dated: September 23, 2014)

The crystal structure and chemical bonding of magnetron-sputtering deposited nickel carbide $\text{Ni}_{1-x}\text{C}_x$ ($0.05 \leq x \leq 0.62$) thin films have been investigated by high-resolution X-ray diffraction, transmission electron microscopy, X-ray photoelectron spectroscopy, Raman spectroscopy, and soft X-ray absorption spectroscopy. By using X-ray as well as electron diffraction, we found carbon-containing hcp-Ni (hcp- NiC_y phase), instead of the expected rhombohedral- Ni_3C . At low carbon content (4.9 at%) the thin film consists of hcp- NiC_y nanocrystallites mixed with a smaller amount of fcc- NiC_x . The average grain size is about 10-20 nm. With the increase of carbon content to 16.3 at%, the film contains single-phase hcp- NiC_y nanocrystallites with expanded lattice parameters. With further increase of carbon content to 38 at%, and 62 at%, the films transform to X-ray amorphous materials with hcp- NiC_y and fcc- NiC_x nanodomain structures in an amorphous carbon-rich matrix. Raman spectra of carbon indicate dominant sp^2 hybridization, consistent with photoelectron spectra that show a decreasing amount of C-Ni phase with increasing carbon content. The Ni $3d$ - C $2p$ hybridization in the hexagonal structure gives rise to the salient double-peak structure in Ni $2p$ soft X-ray absorption spectra at 16.3 at% that changes with carbon content. We also show that the resistivity is not only governed by the amount of carbon, but increases by more than a factor of two when the samples transform from crystalline to amorphous.

PACS numbers:

I. INTRODUCTION

Transition metal carbides are useful in various applications ranging from wear and oxidation resistant protective coatings to low friction solid lubricants [1, 2]. This flexibility is due to the nanocomposite nanocrystalline/amorphous-C structure that governs the coating's properties depending on the amount of amorphous matrix, and crystallite size of the carbide [3, 4]. Early transition metals such as Ti, Zr, and V form strong covalent metal carbon bonds often in cubic crystals in contrast to late transition metals such as Fe and Ni that form less strong Me-C bonds [5]. The late transition metals usually form completely amorphous or mainly amorphous materials with complex nanocrystallites above a threshold value around 20 at%. An important exception is the Ni-C system, where metastable rhombohedral- Ni_3C nanocrystallites are easily formed in a large composition range [6, 7], and it is more difficult to form completely amorphous films [8]. Using RF sputtering [6], partly amorphous $\text{Ni}_{1-x}\text{C}_x$ films with Ni_3C crystallites embedded in an amorphous $\text{Ni}_{1-x}\text{C}_x$ phase have previously been obtained for $x=0.35$ [6]. Amorphous Ni-C films have also been obtained for $x>0.5$ using reactive co-sputtering with CH_4 as a carbon source [7].

Metallic Ni usually has a cubic fcc structure with space group Fm-3m. In addition, the hcp-Ni phase with space group P63/mmc has been reported [9, 10]. Pure hcp-Ni metal is very unstable, and most previous investigations lack a material composition analysis [6,7]. One study

showed that nano-crystallites of hcp-Ni metal could be synthesized, and likely stabilized by carbon, but is easily transformed into fcc-Ni metal when the size extend more than 5 nm [11]. Because both hcp-Ni with space group P63/mmc and Ni_3C with space group R-3cH contain carbon and have very similar crystal structures, most previous work did not experimentally show how to discriminate hcp-Ni from Ni_3C [12,13]. Only recently, Schaefer *et al.* [14] were able to distinguish between hcp-Ni and Ni_3C structures by means of low-angle X-ray diffraction. Schaefer pointed out that all previously reported hcp-Ni contains carbon, and should be described as rhombohedral Ni_3C [13, 14] in a superstructure with interstitially ordered carbon. The superstructure can be approximated by a hexagonal subcell that is nearly identical in size to that of hcp-Ni with lattice constants $a=2.682 \text{ \AA}$, and $c=4.306 \text{ \AA}$ [15].

In this work, we investigate the nanocomposite-to-amorphous structure, and the nature of chemical bonding between Ni, and C for a range of C concentrations ($0.05 \leq x \leq 0.62$) in magnetron sputtered $\text{Ni}_{1-x}\text{C}_x$ films. As a non-equilibrium process, magnetron sputtering may increase the solubility of C into Ni, and the carbide phase of the film structure may be influenced by the total C content. By employing a combination of X-ray diffraction, high-resolution transmission electron microscopy (HR-TEM), X-ray photoelectron spectroscopy (XPS), Raman, and soft X-ray absorption spectroscopy (XAS), we analyze the Ni carbide, and Ni metal-like nanocrystalline to amorphous contributions to the structure, and the depen-

dence on the carbon content. In particular, we identify the crystallization of the Ni-C system into hcp-Ni and fcc-Ni by combining X-ray diffraction (XRD) with HR-TEM for low carbon contents. We show that the samples do not form a superstructure of Ni₃C with ordered carbon as previously thought. XPS characterization gives a quantitative analysis of the compositions of different Ni-C phases with particular emphasis on the variation of the carbon content in the carbide phase. The electrical resistivity of the Ni_{1-x}C_x films is correlated to the amount of C-Ni and C-C bonds, the degree of crystallization, and the total carbon content.

II. EXPERIMENTAL DETAILS

A. Synthesis and deposition

All the investigated films were deposited by dual dc magnetron sputtering in ultra high vacuum (UHV) on single-crystal Si(001) (10x10 mm) substrates. Prior to deposition, the substrates were cleaned in ultrasound baths of acetone and isopropyl alcohol. During deposition, the substrates biased to -50 V, and preheated to 250°C from the back side by a resistive heater built-into the substrate holder. This made it possible to synthesize the films with a high degree of purity, and with precisely tuned composition. The Ni_{1-x}C_x thin films were deposited in an UHV chamber with a base pressure of 10⁻⁹ Pa from a double current regulated 2 inch magnetron setting in an Ar discharge generated at 3.0 mTorr, and with gas flow rate of 30 sccm. The magnetrons were directed towards a rotating substrate holder at a distance of 15 cm. As separate sputtering sources, graphite, and a non-elemental Ni+C target were used (99.999% pure C, and 99.95% pure Ni). To enable the magnetic field from the magnetron to reach the plasma through the ferromagnetic Ni target, a segmented design was used in, which a circular center part of the target was removed, and placed on a graphite plate. In this way, simultaneous sputtering of Ni, and C from the same target was accomplished [4]. The tuning of the film composition was achieved by keeping the graphite target at a constant current of 300 mA, and tuning the current on the Ni target. The resulting thicknesses of the as-deposited coatings were 740 nm ((*x*=0.05), 635 nm ((*x*=0.16), 309 nm ((*x*=0.38), 250 nm ((*x*=0.62) and 200 nm ((*x*=1.0: a-C) as determined by XRR.

B. Characterization

The structural properties of the thin films were determined by high-resolution XRD analysis. In order to avoid diffraction signal from the Si substrate, grazing incidence (GI) XRD measurements were carried out on a PANalytical EMPYREAN using a Cu *K*α radiation source, and a parallel beam geometry with a 2° incidence angle to avoid substrate peaks and minimize the influence of

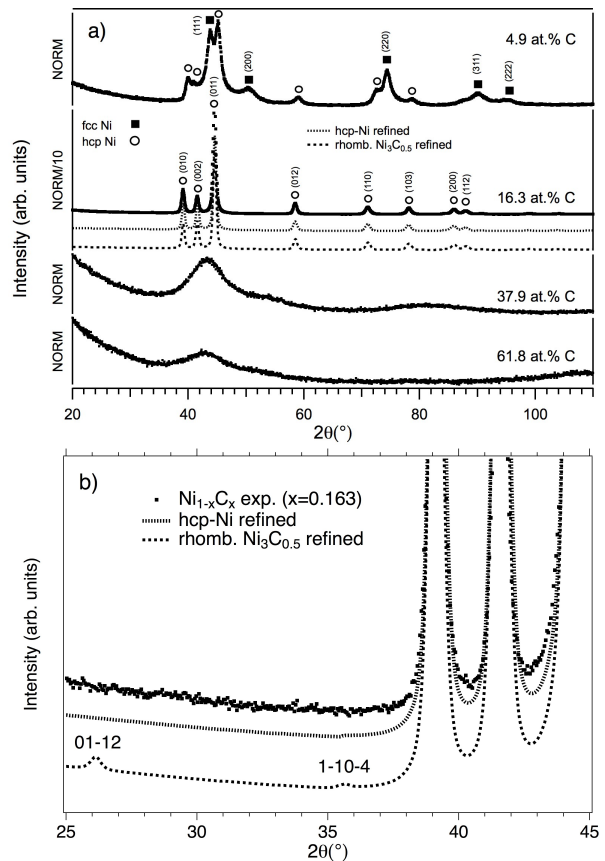


FIG. 1: a) X-ray diffractograms of Ni_{1-x}C_x films with C content ranging from 4.9 at.% to 61.8 at.%. b) Enlargement of the XRD data of the 16.3% C sample at low angles in comparison to Rietveld refinement of hcp-Ni and rhomb. Ni₃C_{0.5} with a similar composition as the 16.3 % sample.

texture. Each XRD scan was performed with 0.1° resolution, 0.05° step length with a total of 1800 points for 6 hours.

HR-TEM, and selected area electron diffraction (SAED) were performed by using a Tecnai G² 20 U-Twin 200 kV FEGTEM microscope. Cross-section samples were mechanically polished, and ion milled to electron transparency by a Gatan Precision Ion Polishing System (PIPS).

The chemical compositions of the films were determined by X-ray photoelectron spectroscopy (XPS) using a Physical Systems Quantum 2000 spectrometer with monochromatic Al *K*α radiation. Depth profiles of the films were acquired by rastered Ar⁺-ion sputter etching over an area of 2x2 mm² with ions being accelerated by the potential difference of 4 kV. The high-resolution scans of the selected peaks were acquired after 6 min, 30 min, 45 min of Ar⁺-ion sputter etching with ions being accelerated by the potential difference of 4 V, 500 V, and 200 kV, respectively. The XPS analysis area was set to a diameter of 200 μm and the step size to 0.05 eV with a base pressure of 10⁻⁹ Pa during all measurements. The

peak fitting was made by Voigt shape functions to account for the energy resolution of the instrument and chemical disorder (Gaussian part) and the lifetime width of the photoionization process (Lorentzian part).

Raman scattering spectroscopy was used in order to correlate the nanostructuring, and sp^2/sp^3 ratio of the films to the carbon concentration. The Raman spectra were acquired at room temperature in the range 800-1900 cm^{-1} in the back scattering configuration using UV 325 nm laser excitation.

X-ray absorption spectroscopy (XAS) measurements were performed in total fluorescence yield (TFY) mode at the undulator beamline I511-3 at MAX II (MAX-IV Laboratory, Lund, Sweden), comprising a 49-pole undulator, and a modified SX-700 plane grating monochromator [16]. The measurements were made at a base pressure lower than $6.7 \cdot 10^{-7}$ Pa. The XAS spectra were measured at 5° grazing incidence angle from the surface plane and a detection angle of 30° from the incident photon direction. All samples were measured in the same geometry with energy resolutions of 0.2, and 0.1 eV at the Ni 2*p*, and C 1*s* absorption edges, respectively. The XAS spectra were normalized to the step before, and after the absorption edges and corrected for background and self-absorption effects [17] with the program XANDA [18] in Fig. 6, and 7.

Cross-sectional scanning electron microscopy (SEM) images were obtained in a LEO 1550 microscope using accelerating voltages of 15 kV in *in-lens* imaging mode. The obtained images were used for thickness measurements, and structural analysis of the coatings.

Sheet resistance measurements were made with a four-point probe “4-dimensions” 280C. For each sample, four readings were made with a different 4-sensor orientation around the center of the sample. As a final value of the electrical resistivity, a mean value over four measurements was made. Each set of measurements on a sample showed similar values indicating negligible influence from surface oxide.

III. RESULTS

A. X-ray diffraction (XRD) and high-resolution transmission electron microscopy (HR-TEM)

Figure 1a shows X-ray diffractograms (XRD) performed to characterize the microstructure of the nickel carbide $\text{Ni}_{1-x}\text{C}_x$ films for $x=0.05, 0.16, 0.38,$ and 0.62 . The XRD data were refined by the Rietveld method using the MAUD program [20]. Five peaks in the top diffractogram ($x=0.05$) are indexed as fcc- NiC_x structure (space group Fm-3m) with a lattice parameter of $a=3.610(1)$ Å. This lattice parameter is larger than that of fcc-Ni metal (3.524 Å) [19], but smaller than that of fcc-NiC (4.077 Å) [20]. Interpolation of these values yield an estimated phase composition of fcc- NiC_x , where $x=0.23-0.30$. However, the lattice parameter also

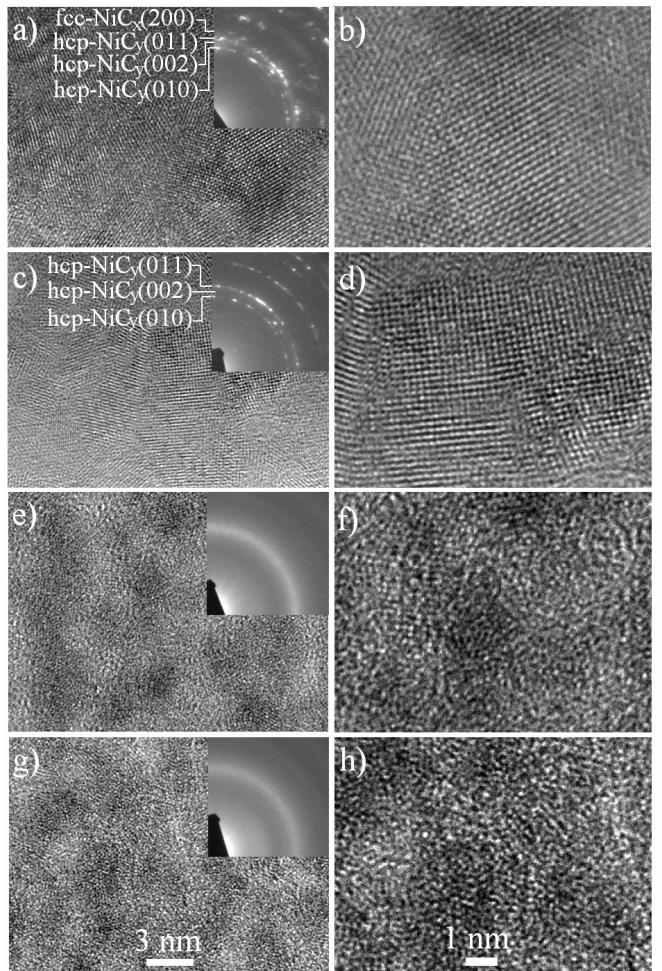


FIG. 2: HR-TEM micrographs of low (left), and high (right) resolution with corresponding SAED patterns for the $\text{Ni}_{1-x}\text{C}_x$ films with increasing x values, top to bottom; a,b) 0.05, c,d) 0.16, e,f) 0.38, and g,h) 0.62. The diffraction rings for the fcc- NiC_x (200) and hcp- NiC_y (011), (002), (010) reflections are indicated in the SAED.

depends on the nano-structured grain size of fcc- NiC_x that has larger cell parameters than in the case of bulk materials. Therefore, $x \leq 0.30$ for fcc- NiC_x in the 0.05 sample, represents an upper limit of the composition.

The other marked reflections in the top diffractogram can be indexed by either hcp-Ni or rhombohedral Ni_3C structures. From a structure point of view, rhombohedral Ni_3C has the same Ni position as hcp-Ni but the ordered interstitial C atoms create additional reflections 01-12 and 1-10-4, which are absent for the hcp-Ni structure. Thus, the rhombohedral structure can be excluded based on the absence of 01-12 and 1-10-4 reflections [21–24]. Furthermore, compared to the pure hcp-Ni phase, the slight peak shift to low angle indicates an expansion of the lattice, due to the carbon occupation. With increasing carbon content, the cell parameters are further

increased (see the second diffractogram of the 16.3 at % C sample in Fig. 1(a)). Thus, the phase with hcp-Ni structure should be termed as hcp-NiC_y (y < 1) instead of hcp-Ni.

The diffractograms are further analyzed with Rietveld refinement. Both hcp-NiC_y and rhombohedral Ni₃C structures were used in the refinement. For comparison, the same carbon content was used for the two structure models, i.e. hcp-NiC_{0.67} and rhombohedral Ni₃C_{0.5}. The refined results in Fig. 1(b) shows that the 01-12 and 1-10-4 peaks are present in rhombohedral Ni₃C_{0.5} but absent in hcp-NiC_{0.67}. The simulated diffractogram of the hcp-NiC_{0.67} agrees well with our experimental data (see Fig. 1(b)). Moreover, the refinement give rise the accurate lattice parameters of hcp-NiC_y as $a=2.611(2)$ Å and $c=4.328(7)$ Å for the 4.9 at% C sample and $a=2.653(7)$ Å, $c=4.337(2)$ Å for the 16.3 at% C sample, respectively. Fig. 1(a) also shows that with increase of carbon content from 4.9 at% to 16.3 at%, the fcc-NiC_x disappears and single phase of hcp-NiC_y forms. Applying Scherrer's equation for the 16.3 at% C sample yield a grain size of 23 nm for all diffraction peaks in agreement with the average grain size in the TEM images. Further increase of carbon content to 37.9 at% and above leads to amorphous-like structures as shown in Fig. 1(a).

The structural evolution of the films with composition is also observed by HRTEM and SAED as shown in Fig. 2. The sharp SAED in Fig. 2c clearly has absence of 012 and 104 reflections, which confirms the hcp-NiC_y structure rather than rhombohedral Ni₃C structure. No significant texture is observed in the SAED. The films with low carbon contents ($x=0.05$, and 0.16) are polycrystalline, and the sharp dots of reflections in the corresponding SAED pattern show that the film with 16.3 at% C consists of hcp-NiC_y, while the film with 4.9 at% C contains two phases: hcp-NiC_y, and cubic fcc-NiC_x (the 200 reflection is consistent with XRD). In contrast, the films with higher carbon contents (38, and 62 at% C) consist of Ni-rich nanocrystalline domains surrounded by amorphous carbon-rich matrix domains. The average grain size of the nanocrystalline domains is approximately 3-5 nm ($x=0.38$, and 0.62). Although it is difficult to identify the exact phases for these X-ray amorphous samples with high carbon content, the XRD peak intensity distribution profiles indicate that the strongest broad structure at $2\theta=42.6^\circ$ includes both hcp-NiC_y 010, 002 and 011 reflections, and a fcc-NiC_x 111 reflection, respectively. The broad structure at $2\theta=82^\circ$ is formed by fcc-NiC_x 200, and hcp-NiC_y 110 and 103 reflections. Thus, as observed by the HR-TEM in Fig. 2, the samples with high carbon contents of 38, and 62 at% likely consist of both cubic fcc-NiC_x, and hcp-NiC_y nanocrystallites both with a small grain size approximately 3-5 nm.

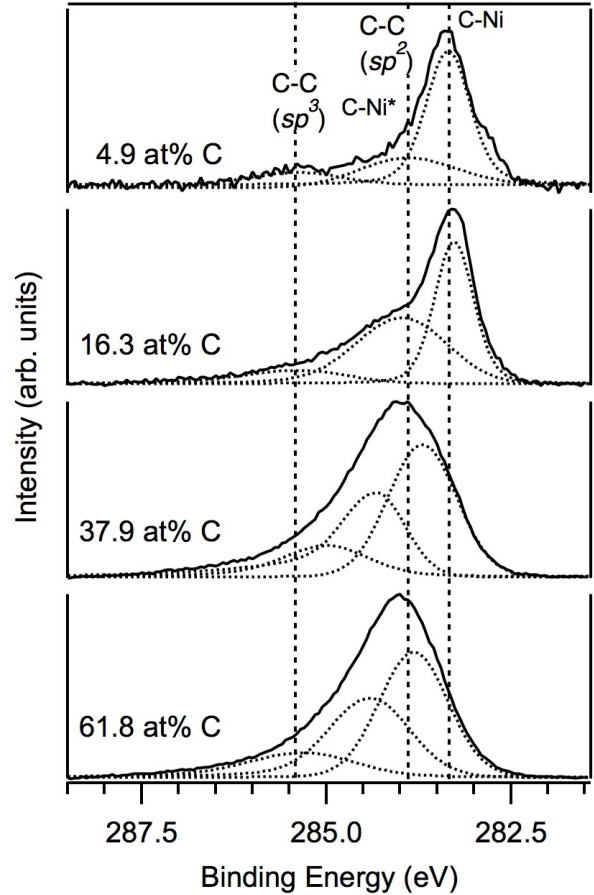


FIG. 3: C 1s XPS spectra of the Ni_{1-x}C_x films with carbon content ranging from 5 at.% to 62 at.%. The deconvoluted peaks at 283.3, and 285.3 eV, indicated by the dashed vertical lines correspond to carbidic NiC carbon in Ni-C bonds, and free carbon in C-C bonds, respectively. A third structure is identified at 283.9 eV, and can be associated with charge-transfer C-Ni* bonds or C-C in sp^2 hybridized bonds.

B. X-ray photoemission spectroscopy (XPS)

Figure 3 shows C 1s core-level XPS spectra of the four Ni_{1-x}C_x films with $x=0.05$, 0.16 , 0.38 , and 0.62 . As observed, at least three peaks are required to deconvolute the spectra. A peak at 283.3 eV can be assigned to Ni-C bonds, while a second peak at 285.3 eV can be assigned to sp^3 hybridized carbon (C-C- sp^3) [25, 26]. Between these two peaks, a third feature is clearly present. The intensity of the middle peak increases with carbon content and is also shifted from about 283.9 eV for the most Ni-rich film to about 284.5 eV in the most C-rich film. Most likely, several types of carbon is contributing to this feature. Firstly, sp^2 -hybridized carbon is known to exhibit a peak at about 0.9 eV lower binding energy than sp^3 -hybridized carbon, i.e. at about 284.0 eV [25]. It is well known that binary sputter-deposited metal car-

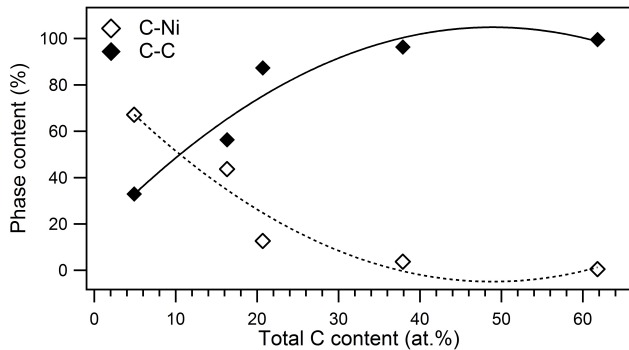


FIG. 4: Relative amount of C-Ni, and C-C bonds determined as the proportions of the areas fitted on the XPS C $1s$ peak. The two curved lines are guidelines for the eye.

bide films often are nanocomposites with a carbide phase in an amorphous carbon (a-C) matrix. Previous C $1s$ XPS studies on the a-C phase have shown a mixture of sp^2 - and sp^3 -hybridized carbon. Consequently, it is most likely that a part of the intensity of the feature at 283.9-284.5 eV originates from free carbon in an a-C matrix. Secondly, studies on sputter-deposited Me-C films have also shown an additional Me-C feature at a slightly higher binding energy [3] that can be due to sputter damage of the metal carbide grains. Thirdly, a contribution originates from surface Me atoms in the carbide grains. This is caused by charge-transfer effects where charge is transferred from the metal surface atoms to the more electronegative carbon atoms in the a-C matrix [7]. In nanocomposites with very small grains or domains, the relative amount of surface atoms is large and will show up as a high-energy shoulder on the main C $1s$ Me-C peak (denoted Me-C*) [9]. However, for the $Ni_{1-x}C_x$ films, it is impossible to deconvolute the feature at 283.9-284.5 eV into separate C-C (sp^2) and Ni-C* peaks. However, a comparison with Ti-C, Cr-C and Fe-C films show that the Me-C* contribution is small in XPS compared to the C-C (sp^2) peak [27, 28]. For this reason, we assign the entire peak at 283.9-284.5 eV to C in a-C, although it will give a slight overestimation of the amount of the C-C (sp^2) phase compared to the NiC carbide phases. The XPS data supports the TEM and XRD studies and confirms that the films consist of at least two phases; fcc- NiC_x and hcp- NiC_y carbide nanocrystallites dispersed in an amorphous carbon (a-C) phase. The intense C-Ni peak for $x=0.05$ and 0.16 is an indication of the localized character of the Ni-C bonds in the nanocrystallites.

Figure 4 shows the relative amount of the carbide and a-C phases as a function of total carbon content (assuming that the Ni-C* contribution to 283.9-284.5 eV peak can be neglected). As can be seen, the relative amount of the a-C phase increases non-linearly with the total carbon content. The total composition analysis in Table I is valid under the assumption that the total photoemission cross section in all the samples is constant for carbon.

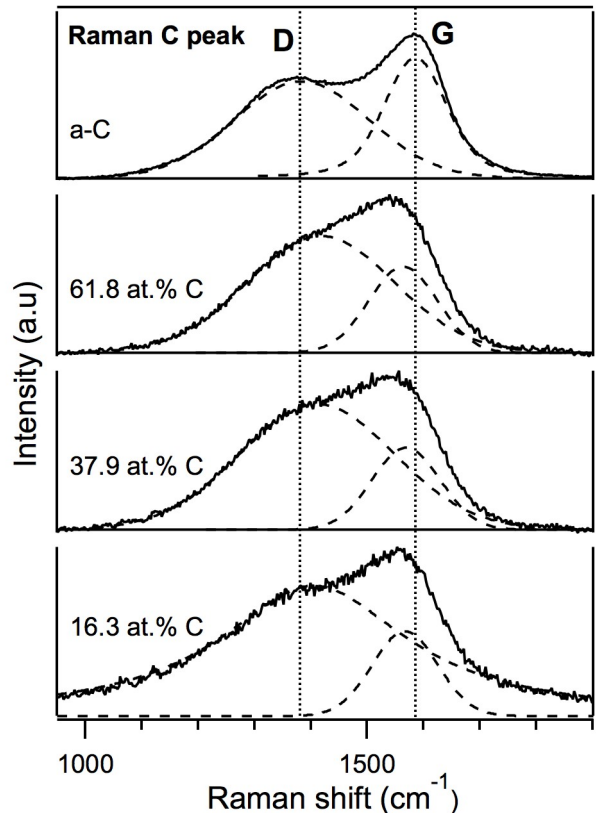


FIG. 5: Raman spectra for the carbon peak of the $Ni_{1-x}C_x$ films for $x=0.16$, 0.38, 0.62, and amorphous carbon (a-C). The two vertical dashed lines indicate the disorder (D), and graphite (G) peaks of the fitted peak components [29, 30].

The combined carbon in the fcc- NiC_x and hcp- NiC_y carbide phases can now be estimated using the data in Fig. 4 as presented in Table I. The analysis show that the carbon content of the carbide phase strongly increase with the total carbon content from 15.7 at% (0.16 at% total), 36 at% (0.38 at% total) to 60 at% (0.62 at% total). However, the estimated carbon content in the carbide phase represents a lower limit since the contribution of Ni-C* has been neglected in the analysis of the C $1s$ spectra. The variation of the carbon content in the NiC carbide phase is consistent with the small dispersion of the Ni $2p_{3/2}$ XPS peak position from 852.7 eV ($x=0.05$), 852.9 eV ($x=0.16$), 853.0 eV ($x=0.38$), to 853.1 eV ($x=0.62$).

C. Raman spectroscopy

Figure 5 shows carbon Raman spectra of the $Ni_{1-x}C_x$ films with x values of 0.16, 0.38, and 0.62, in comparison to pure amorphous carbon (a-C). As the Raman scattering cross section from C-Ni is low, the Raman spectra are dominated by the segregated part of the carbon in the compounds. The two band components in the spec-

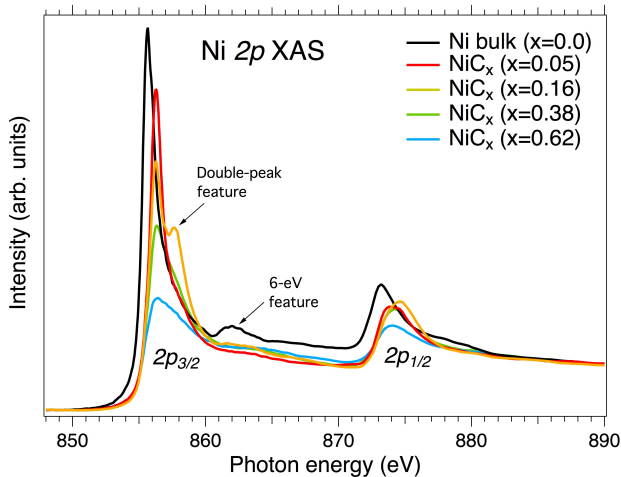


FIG. 6: (Color online) Ni 2p TFY-XAS spectra of $\text{Ni}_{1-x}\text{C}_x$ for different C contents in comparison to bulk Ni ($x=0.0$).

tra, the disordered (D), and graphite (G) peaks, were deconvoluted by Voigt shape functions. In pure graphite, the vibrational mode that gives rise to the G-band is known to be due to the relative motion of sp^2 hybridized C atoms while the D band is due to the breathing vibrational mode of the six-membered rings [29]. The energies of the D, and the G bands have an almost constant position around 1410 cm^{-1} , and 1570 cm^{-1} , respectively. Both peaks are slightly shifted together with respect to their positions for the pure a-C of 1384 cm^{-1} , and 1585 cm^{-1} respectively. The I_D/I_G height ratios of the films are 1.53, 1.59, 1.36 while for the a-C film, the ratio is lower (0.87) due to a more graphitic character of the carbon bonds [30]. These ratios approximately correspond to sp^2 fractions of 0.68, 0.70, 0.65 while it is lower for a-C (0.59). The predominant sp^2 hybridization is consistent with the observations in the XPS spectra of the same samples.

D. Ni 2p X-ray absorption spectroscopy

Figure 6 shows Ni 2p XAS spectra of the $3d$, and $4s$ conduction bands following the Ni $2p_{3/2,1/2} \rightarrow 3d$ dipole transitions of the $\text{Ni}_{1-x}\text{C}_x$ films with different carbon content in comparison to Ni metal. The Ni 2p XAS spectra mainly represent the nickel contribution in the fcc- NiC_x and hcp- NiC_y carbide phases. The main peak structures are associated with the Ni $2p_{3/2}$ and the $2p_{1/2}$ core-shell spin-orbit splitting of 17.3 eV. A comparison of the spectra shows four interesting effects: (i) the intensity of the the main $2p_{3/2}$ peak decrease with carbon content. The Ni 2p XAS intensity is proportional to the unoccupied $3d$ states, and the intensity trend indicates that the Ni $3d$ electron density decreases around the absorbing Ni atoms for higher carbon concentration. The intensity of the normally sharp Ni $2p_{3/2}$ XAS peak in

pure crystalline Ni phase, is largely suppressed by the broadening and distribution of different types of chemical bonds. (ii) For comparison, the XAS spectrum of fcc Ni metal ($x=0.0$) has narrower, and more intense $2p_{3/2}$, and $2p_{1/2}$ absorption peaks, whereas the XAS spectra of the carbon-containing films are broader and shifted by 0.6 eV towards higher photon energy. This energy shift is an indication of higher ionicity of Ni as a result of charge-transfer from Ni to C. (iii) For $x=0.16$, a pronounced double-peak structure with 1.4 eV splitting from the main peak at the $2p_{3/2}$ peak is observed. The double-peak feature is similar to the $t_{2g}-e_g$ crystal field splitting observed in TiC nanocomposites [16]. It is a signature of a change in orbital occupation to the hcp crystal structure while the sharp single-peak feature of Ni metal is a signature of fcc structure (cubic). For $x=0.05$, the double-peak structure has essentially vanished in comparison to at $x=0.16$ due to the superposition of the strong fcc contribution. (iv) The 6-eV feature [19, 31] above the main $2p_{3/2}$ peak is prominent in Ni metal ($x=0.0$) that is associated with electron correlation effects and narrow-band phenomena [32]. The intensity of the 6-eV feature is very low in the $\text{Ni}_{1-x}\text{C}_x$ films in comparison to Ni metal even at $x=0.05$ due to more delocalized bands.

A comparison of the spectral shapes at different carbon contents shows that the $2p_{3/2}/2p_{1/2}$ branching ratio estimated by the peak height is largest (3.0) for the lowest carbon content ($x=0.05$) and is similar as for Ni metal. With increasing carbon content, the branching ratio decreases to 2.3 ($x=0.16$), 1.8 ($x=0.38$) and 1.3 ($x=0.62$). Integration of peak areas by Gaussian functions give the same trend as comparison of the the peak heights but yield a higher branching ratio for Ni metal than for the other samples. A lower $2p_{3/2}/2p_{1/2}$ branching ratio is an indication of higher ionicity (lower conductivity) for the highest carbon content [33–35]. However, the $2p_{3/2}/2p_{1/2}$ branching ratio is a result of the ionicity for Ni, mainly in the fcc- NiC_x and hcp- NiC_y carbide components, and not for the entire film. For the higher carbon contents, when the main part of the film consists of C-rich matrix areas, this phase determines the resistivity.

E. C 1s X-ray absorption spectroscopy

Figure 7 shows C 1s XAS spectra of the $\text{Ni}_{1-x}\text{C}_x$ films probing the unoccupied C $2p$ conduction bands as a superposition of the NiC carbide phases, and the changes in the C matrix phase with composition. The first peak structure (1) at $\sim 285\text{ eV}$ is associated with empty π^* states, and the higher states (3-6) above 290 eV are associated with unoccupied σ^* states. The empty π^* orbitals (1) consists of the sum of two contributions in $\text{Ni}_{1-x}\text{C}_x$: (i) sp^2 (C=C), and sp^1 hybridized C states in the amorphous carbon phase, and (ii) C $2p$ - Ni $3d$ hybridized states in the fcc- NiC_x and hcp- NiC_y carbide phases. The peak at $\sim 288.5\text{ eV}$ is also due to C $2p$ - Ni

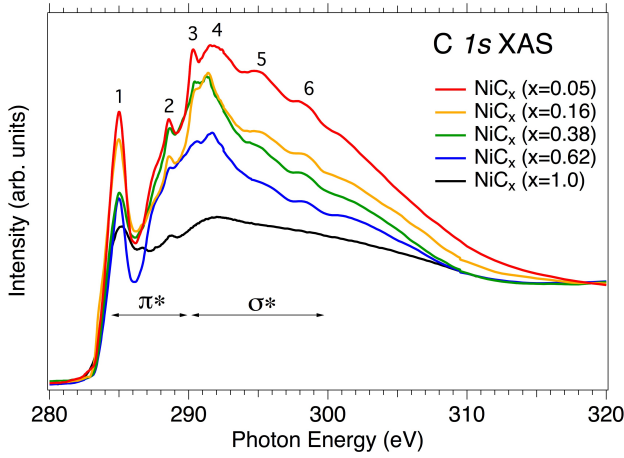


FIG. 7: (Color online) C 1s TFY-XAS spectra of $\text{Ni}_{1-x}\text{C}_x$ for different C contents compared to amorphous carbon (a-C, $x=1.0$).

$3d$ hybridization with a superimposed contribution from the carbon phase [16]. The energy region above 290 eV is known to originate from sp^3 hybridized (C-C) σ^* resonances, where the peak (4) at 291.5 eV forms a shape resonance with multielectron excitations towards higher energies [16]. The most intense structure shows highest intensity for $x=0.05$ that originates from sp^3 hybridized σ^* states. Additional σ^* states (5), (6) at 295 eV and 298 eV are also associated with sp^3 bonding. Contrary to the case of TiC [16], there is no pre-peak below the π^* peak at 283.3 eV for NiC.

The integrated $\pi^*/[\pi^*+\sigma^*]$ intensity ratio was calculated by fitting a step-edge background with a Gaussian function to each peak following the procedure in Refs. [36, 37] in order to not overestimate the σ contribution. We assumed that π^* peaks occur below and σ^* peaks above 290 eV as indicated in Fig. 7. This analysis method gives an estimation of the relative amount of π^* (sp^2 , sp^1 hybridization content) in the samples as shown in Table I. The fraction of sp^2 is smallest for $x=0.05$ and highest for a-C, following a similar trend as the XPS and the Raman results.

F. Resistivity measurements

Figure 8a shows the electrical resistivity in the $\text{Ni}_{1-x}\text{C}_x$ films as a function of carbon content x . Compared to the electrical resistivity of $6.93 \mu\Omega\text{cm}$ [38] for Ni metal, the small introduction of C of ~ 3 at.% increases the resistivity to $\sim 30 \mu\Omega\text{cm}$. However, it is well known that metallic thin films display higher electrical resistivity compared to the bulk metals [38, 39]. When increasing the C content another 2 at.% C, the resistivity doubles to $\sim 62 \mu\Omega\text{cm}$, and continues approximately linearly to $\sim 150 \mu\Omega\text{cm}$ at 16.3 at.% C. Above this carbon

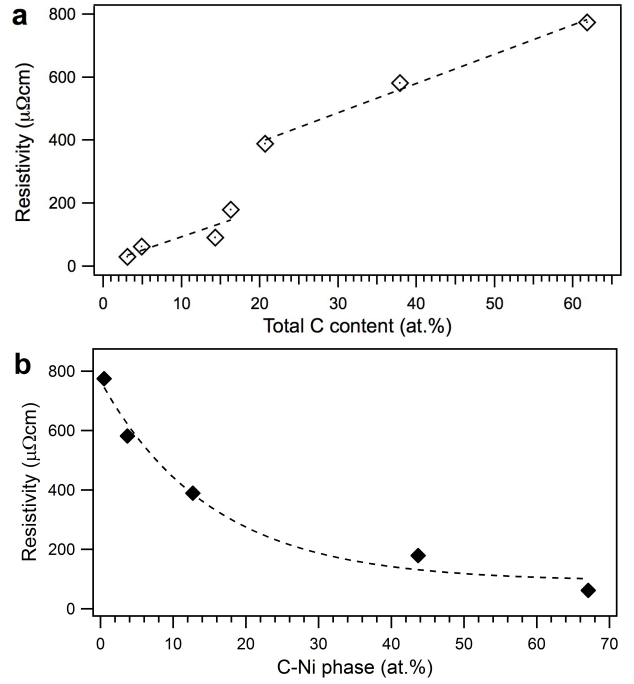


FIG. 8: a) Resistivity of the $\text{Ni}_{1-x}\text{C}_x$ films depending on the C content as determined from sheet resistance measurements by a four-point probe and film thickness determined by SEM. b) The resistivity is plotted as a function of the relative amount of C bound in the C-Ni bonds. The dashed least-square fitted curves are guides for the eye.

content, the samples transform from polycrystalline to amorphous and the resistivity increases by more a factor of two to $\sim 400 \mu\Omega\text{cm}$. Above 20.7 at% C, the resistivity increases approximately linearly up to a maximum value of $\sim 775 \mu\Omega\text{cm}$ for the C content of 61.8 at.%. The increase of electrical resistivity with increasing C content in the films is correlated to the increased amount of C-C bonding (Fig. 4), and the interstitial incorporation of inter-bonded C atoms between the Ni lattice sites forming the fcc- NiC_x and hcp- NiC_y carbide phases. The a-C phase is known to be a very poor conductor compared to Ni metal. As the XPS analysis shows contributions from C-C bonds for all the investigated films, an increase of resistivity is not only governed by the increase of the amorphous C phase but is also influenced by the crystallinity. Fig. 8b shows the exponential decrease of electrical resistivity with the increasing proportion of the NiC carbide phases. The symmetry of the C-Ni component of the C 1s XPS peak also suggests a low electrical conductivity of the carbide. However, as shown by the XPS analysis, there is only a small amount of C incorporated into Ni. Therefore, the NiC phases could be regarded as a solid solution [39, 40] with low amount of C solved into Ni rather than as an ordinary carbide phase. Thus, the C-Ni component of the structure is mostly metallic, leaving the a-C matrix phase to determine the general trend in the electrical resistivity of the films.

TABLE I: Composition of the Ni-C films for $x=0.05, 0.16, 0.38,$ and 0.62 . The amount of carbon in the carbide phase and the sp^2 fractions were determined by integrating the areas under the corresponding peak structures in C $1s$ XPS spectra. The sp^2 fractions in Raman were estimated from Ref. 28.

Total composition	Ni _{0.95} C _{0.05}	Ni _{0.84} C _{0.16}	Ni _{0.62} C _{0.38}	Ni _{0.38} C _{0.62}	a-C
at% C in NiC _y phase	5.0	15.7	36	60	100
XPS sp^2 fraction	0.64	0.80	0.69	0.70	–
Raman sp^2 fraction	–	0.77	0.79	0.89	0.71
C $1s$ XAS $\pi^*/[\pi^*+\sigma^*]$	0.42	0.53	0.60	0.56	0.72

IV. DISCUSSION

The most significant difference between Ni_{1-x}C_x as compared to other late transition-metal carbides such as Cr_{1-x}C_x [4], and Fe_{1-x}C_x [41], is the precipitation of Ni-based phases in the form of nanocrystals, while Cr, and Fe form mainly completely amorphous films for a large range of compositions. In our combined analysis of XRD, and HR-TEM, we find that at low carbon content ($x=0.05$), the Ni_{1-x}C_x films consist of hcp-NiC_y nanocrystals with a smaller contribution (25-30%) of fcc-NiC_y nanocrystals, where $y \leq 0.30$. For low carbon contents ($x=0.05$ and 0.16), the estimated average grain size is relatively large, 10-20 nm.

Previous investigations of hcp-Ni nanocrystals are lacking a material composition analysis [6, 7], but pure hcp-Ni metal is known to be unstable or metastable. To our knowledge, only one previous experiment showed that crystallites of hcp-Ni metal could be synthesized, and it was easily transformed into fcc-Ni metal when its size was larger than 5 nm [11]. Most of the reported hcp-Ni metals are likely stabilized by carbon. The Ni atom in rhombohedral-Ni₃C and hcp-Ni structures occupy exactly the same positions and yield identical XRD data at high angle ($>38^\circ$) and, this is the reason why it has not been identified before. Recently, Schaefer *et al.* pointed out that it is possible to experimentally distinguish hcp-Ni and rhombohedral-Ni₃C structures by using low-angle XRD. In addition, He and Schaefer claimed that there exists no hcp-Ni because they inferred that all the previously reported hexagonal Ni carbides contained carbon, presented 01-12 and 1-10-4 reflections, and should therefore be described as rhombohedral Ni₃C [13, 14]. However, in our sputter-deposited Ni_{1-x}C_x samples, the absence of 01-12, and 1-10-4 reflections indicates that the superstructure of rhombohedral Ni₃C is not formed, and instead, a hcp-Ni structure occurs. It should be noted that our hcp-Ni structure does contain C and its cell parameters depend on the carbon content. This is consistent with previous works, showing that hcp-Ni is stabilized by carbon. Thus, our hcp-Ni phase should be described as hcp-NiC_y instead of hcp-Ni or rhombohedral-Ni₃C_{1-x}. Uhlig *et al.* also found a carbon containing Ni structure [9]. However, the absence of low-angle reflec-

tions indicates that their films consists of hcp-Ni with a carbon content rather than Ni₃C.

The XPS and XAS measurements confirm the structure to be carbidic and do not show spectral profiles of metallic Ni. From a structural point of view, the difference between hcp-Ni₃C and rhombohedral Ni₃C is the carbon position: ordered interstitial C in rhombohedral Ni₃C and disordered interstitial C in hcp-Ni₃C. The formation of hcp-NiC_y instead of rhombohedral-Ni₃C may be due to the non-equilibrium sputtering process. Moreover, at low carbon content, hcp-NiC_y or rhombohedral-Ni₃C is likely more stable than fcc-NiC_x. Further theoretical calculations will be performed to verify this hypothesis, and consequently give an interpretation why NiC_x form crystalline phases, whereas CrC_x and FeC_x form amorphous phases at low carbon content.

The difference in XPS binding energy of the C-Ni peak in comparison to the C-C peak (2.0 eV) is due to the different types of bonding environments. A small low-energy shift of 0.15 eV between the samples with 4.9 at% C. This observation is consistent with a small XPS high-energy shift of 0.25 eV at the Ni $2p_{3/2}$ edge for these crystalline samples. As the structure of the samples change from crystalline to amorphous at 38 and 62 at% C, one would also expect a smaller chemical shift in the case of Ni carbides. This scenario with a smaller chemical shift for the late transition metal carbides is consistent when comparing to Ti-C (2.5 eV) [5] but not for Fe-C (1.7 eV) [41] and Cr-C (1.5 eV) [3], where it is smaller. In this respect, XAS gives important complementary information to XPS about charge-transfer effects. The general intensity trend in the $2p$ branching ratio of the Ni XAS spectra is a signature of charge-transfer from Ni to C that is largest for the sample that contains most C (i.e., $x=0.62$). The variation in intensity of the unoccupied states reflects changes in orbital occupation and bonding of the atoms at the carbide/matrix interface between crystallites, and amorphous domains. It can be assumed that charge-transfer occurs within the fcc-NiC_x and hcp-NiC_y nanocrystal carbide phases, but more significant across the carbide/matrix interface with the surrounding amorphous C-phase or between nanocrystals, that depends on the nanocrystalline size.

Moreover, the 6-eV feature in the Ni XAS spectra that signifies electron correlation effects and narrow-band

phenomena in metallic Ni [19, 31] is washed out in the $\text{Ni}_{1-x}\text{C}_x$ samples due to the Ni $3d$ -C $2p$ orbital overlap that changes the properties of Ni already at very low carbon content. Thus, the spectral profiles of the $\text{Ni}_{1-x}\text{C}_x$ samples exhibit carbide signatures and exclude metallic nickel. Furthermore, for the carbon content of $x=0.16$, the ligand-field type of splitting by 1.4 eV that occurs in Ni XAS signifies a change in the local coordination and orbital occupation with the formation of the single-phase hcp- NiC_y carbide phase. The most stable NiC phase is cubic [15], but from the combined shape of the Ni $2p$ (no crystal-field splitting) and C $1s$ XAS spectra (absence of pre-peak), this is excluded and consistent with the XRD observations. Using surface-sensitive TEY measurements, Choo *et al.* [42] associated the double-structure in Ni $2p$ XAS of hcp Ni with surface oxidation. With bulk-sensitive TFY-XAS, we find that this feature is due to the intrinsic hcp Ni structure.

Since charge-transfer effects are clearly observed in bulk-sensitive XAS, this contribution is also expected in the more surface sensitive XPS spectra. Although this contribution is difficult to separate in the XPS data, part of the third peak between the C-C, and C-Fe peaks should be associated with charge-transfer effects at the interfaces between nanocrystals. The size and the number of fcc- NiC_x and hcp- NiC_y nanocrystals affect the amount of interface, and charge-transfer between the domains. As observed by the XPS analysis, we find that the carbon content in the carbide phase varies significantly with the total carbon content (Table I). However, the amount of sp^2 -fraction (0.6-0.8) as observed in XPS, Raman and XAS is higher in all samples in comparison to a-C and does not change significantly when the samples transform from crystalline to amorphous. On the other hand, the trend in the resistivity depends on the carbon content as well as the crystallinity. To energetically explain why particular nanocrystals form in the Ni-C system and not in other late transition metal carbides, further experimental and theoretical work will be carried out including the effect of magnetic properties.

V. CONCLUSIONS

Magnetron sputtered nanocomposite $\text{Ni}_{1-x}\text{C}_x$ films were investigated for a large composition range

($0.05 \leq x \leq 0.62$). We discovered a novel hcp- NiC_y phase, and show how it is different from rhombohedral Ni_3C . At low carbon content (4.9 at%), the $\text{Ni}_{1-x}\text{C}_x$ film consists of hcp- NiC_y and fcc- NiC_x nanoparticles with an average grain size of 10-20 nm as observed by high-resolution X-ray diffraction and transmission electron microscopy. With increasing carbon content (16 at%), single-phase hcp- NiC_y is formed also with an average grain size of 10-20 nm. A double structure in the X-ray absorption spectra reveals a change in the orbital occupation and bonding for hcp- NiC_y in comparison to the other samples. Further increase of carbon content to 38 at%, and 62 at%, transforms the films to complex X-ray amorphous materials with a mixture of randomly-oriented short-range ordered hcp- NiC_y and fcc- NiC_x nanodomain structures surrounded by an increasing amount of amorphous carbon-rich matrix. X-ray photoelectron and X-ray absorption spectroscopy analyses reveal that interbonding states between the nanocrystallites, and domain structures represent a third type of phase that increases with carbon content. The general trend of increased electrical resistivity with increasing carbon content in the films is correlated to the increased amount of C-C bonding observed in X-ray photoelectron spectroscopy. As the C-Ni phase component of the structure is metallic, the carbon matrix phase determines the electrical resistivity of the films when the films are amorphous. We also find an increase of the resistivity by more than a factor of two when the samples transform from crystalline to amorphous.

VI. ACKNOWLEDGEMENTS

We would like to thank the staff at the MAX IV Laboratory for experimental support, and Jill Sundberg, UU, for help with the Raman measurements. The work was supported by the Swedish Research Council (VR) Linnaeus, and Project Grants. M. M., U. J. and J. L. also acknowledges support from the SSF synergy grant *FUNCASE* Functional Carbides and Advanced Surface Engineering.

**Corresponding author: Martin.Magnuson@ifm.liu.se

-
- [1] A. Cavaleiro and J. Th. M DeHosson, (ed) *Nanostructured Coatings* (Berlin: Springer) 2006.
 - [2] Y.Q. Cheng, E. Ma; *Progress in Materials Science* **56**, 379-473 (2011).
 - [3] M. Andersson, J. Höglström, S. Urbonaite, A. Furlan, L. Nyholm and U. Jansson; *Vacuum* **86** 1408 (2012).
 - [4] M. Magnuson, M. Andersson, J. Lu, L. Hultman and U. Jansson; *J. Phys.: Condens. Matter* **24**, 225004 (2012).
 - [5] U. Jansson and E. Lewin; *Thin Solid Films* **536**, 1 (2013).
 - [6] N. Laidani, L. Calliari, G. Speranza, V. Micheli and E. Galvanetto; *Surf. Coat. Technol.* **100-101**, 116 (1998).
 - [7] J. Shi, Y. Hashiba and O. Nittono; *J. Materials Sci* **36**, 343 (2001).
 - [8] E. Bauer-Grosse and A. Aouni; *J. of Non-Crystalline Solids* **353**, 3644 (2007).
 - [9] S. Uhlig, R. Struis, H. Schmid-Engel, J. Bock, A.-C. Probst, O. Freitag-Weber, I. Zizak, R. Chernikov, G. Schultes; *Diamond & Relat Mat.* **34**, 25 (2013).

- [10] R. Kopplert et al. *Diamond and Relat. Mat.* **25**, 50 (2012).
- [11] W. Tian, H.P. Sun, X.Q. Pan, J.H. Yu, M. Yeadon, C.B. Boothroyd, Y.P. Feng, R.A. Lukaszew, R. Clarke; *Appl. Phys. Lett.* **86**, 131915 (2005).
- [12] B. Ingham, N. Gaston, K. Fahy, X. Y. Chin, C. J. Dotzler, E. Rees, G. Haslam, Z. H. Barber, G. T. Burstein, and M. P. Ryanet; *J. Phys. Chem. C* **116**, 6159 (2012).
- [13] L. He; *J of Magnetism and Magnetic Materials*, **322** 1991 (2010).
- [14] Z. L. Schaefer, Weeber KM, Misra R, Schiffer P and Schaak RE, *Chemistry of Materials*
- [15] B. Jacobson and A. Westgren; *Z. Phys. Chem. Abt. B* **20**, 361 (1933).
- [16] M. Magnuson, E. Lewin, U. Hultman and U. Jansson; *Phys. Rev. B* **80**, 235108 (2009).
- [17] M. Magnuson, N. Wassdahl and J. Nordgren; *Phys. Rev. B* **56**, 12238 (1997).
- [18] K.V.Klementev; *J. Phys. D: Appl. Phys.* **34**, 209-17 (2001); XANES dactyloscope for Windows, K. V. Klementiev, freeware: www.desy.de/~klmn/xanda.html www.cells.es/old/Beamlines/CLAESS/software/
- [19] M. Magnuson, N. Wassdahl, A. Nilsson, A. Föhlisch, J. Nordgren and N. Mårtensson; *Phys. Rev. B* **58**, 3677 (1998).
- [20] L. Lutterotti, *Nuclear Instruments and Methods in Physics Research B* **268**, 334 (2010).
- [21] I. K. Suh, H. Ohta and Y. Waseda; *J. of Materials Science* **23** 757 (1988).
- [22] Gibson JS, Uddin J, Cundari TR, Bodiford NK and Wilson AK; *J of Physics: Condensed Matter* **22**, 4455031 (2010).
- [23] S. Nagakura; *J. Phys. Soc. Jpn.* **13**, 1005 (1958).
- [24] S. D. Wijeyesekera and R. Hoffmann; *Organometallics*, vol. **3**, 949 (1984).
- [25] J. Diaz, G. Paolicelli, S. Ferrer and F. Comin; *Phys. Rev. B* **54**, 8064 (1996).
- [26] Gy. J. Kovacs *et al.* *Thin Solid Films* **516**, 7942 (2008).
- [27] C. Popov *et al.* *Diamond and Relat. Mat.* **13**, 2071 (2004).
- [28] J. I. B. Wilson *et al.*; *J. Elec Spec.* **121**, 183 (2001).
- [29] A.C. Ferrari, J. Robertson; *Phys. Rev. B* **61**, 14095-14107 (2000).
- [30] J. Schwan, S. Ulrich, V. Batori, H. Ehrhardt and S. R. P. Silva; *J. Appl. Phys.* **80**, 440 (1996).
- [31] M. Magnuson, A. Nilsson, M. Weinelt, and N. Mårtensson; *Phys. Rev. B* **60**, 2436 (1998).
- [32] M. Magnuson, S. M. Butorin, A. Agui and J. Nordgren; *J. Phys. Condens. Matter* **14**, 3669 (2002).
- [33] M. Magnuson, O. Wilhelmsson, M. Mattesini, S. Li, R. Ahuja, O. Eriksson, H. Högborg, L. Hultman and U. Jansson; *Phys. Rev. B* **78**, 035117 (2008).
- [34] M. Magnuson, O. Wilhelmsson, J.-P. Palmquist, U. Jansson, M. Mattesini, S. Li, R. Ahuja and O. Eriksson; *Phys. Rev. B* **74**, 195108 (2006).
- [35] R. Laskowski and P. Blaha; *Phys. Rev. B* **82**, 205104 (2010).
- [36] J. Diaz, S. Anders, X. Zhou, E. J. Moler, S. A. Kellar and Z. Hussain; *Phys. Rev. B* **64**, 125204 (2001).
- [37] A. Saikubo, K. Kanda, M. Niibe and S. Matsui; *New Diamond and Frontier Carbon Techn.* **16**, 235 (2006).
- [38] *CRC Handbook of Chemistry and Physics*, CRC Press, 92nd Edition, (2011); <http://www.hbcbnetbase.com>
- [39] V. K. Portnoi, A. V. Leonov, S. N. Mudretsova and S. A. Fedotov; *The Physics of Metals and Metallography*; **109**, 153 (2010).
- [40] S. I. Ryabtsev, V. F. Bashev, A. I. Belkin and A. S. Ryabtsev; *The Physics of Metals and Metallography*; **102**, 305 (2006).
- [41] A. Furlan, J. Lu, U. Jansson, L. Hultman and M. Magnuson; submitted.
- [42] S. Choo, K. Lee, Y. Jo, S.-M. Yoon, J.-Y. Choi, J.-Y. Kim, J.-H. Park, K.-J. Lee, J.-H. Lee and M.-H. Jung; *J. Nanoscience and Nanotechnology* **11**, 6126 (2011).